

Dynamics of zero-Prandtl number convection near onset

Supriyo Paul,^{1,a)} Pinaki Pal,² Pankaj Wahi,^{3,b)} and Mahendra K. Verma^{1,c)}

¹Department of Physics, Indian Institute of Technology, Kanpur 208 016, India

²Department of Mathematics, National Institute of Technology, Durgapur 713 209, India

³Department of Mechanical Engineering, Indian Institute of Technology, Kanpur 208 016, India

(Received 1 October 2010; accepted 26 April 2011; published online 13 June 2011)

We present a detailed bifurcation scenario of zero-Prandtl number Rayleigh-Bénard convection using direct numerical simulations (DNS) and a 27-mode low-dimensional model containing the most energetic modes of DNS. The bifurcation analysis reveals a rich variety of convective flow patterns and chaotic solutions, some of which are common to that of the 13-mode model of Pal *et al.* [EPL 87, 54003 (2009)]. We also observed a set of periodic and chaotic wavy rolls in DNS and in the model similar to those observed in experiments and numerical simulations. The time period of the wavy rolls is closely related to the eigenvalues of the stability matrix of the Hopf bifurcation points at the onset of convection. This time period is in good agreement with the experimental results for low-Prandtl number fluids. The chaotic attractor of the wavy roll solutions is born through a quasiperiodic and phase-locking route to chaos. © 2011 American Institute of Physics. [doi:10.1063/1.3591793]

Rayleigh-Bénard convection (RBC) is an idealized version of thermal convection in which a fluid layer confined between two conducting plates is heated from below. Nature of convective flow depends critically on Prandtl number P and Rayleigh number R . One of the key problems in this field is the $P=0$ (zero- P) limit that shows three-dimensional flow patterns and chaotic behaviour just at the onset of convection. The chaotic attractor subsequently bifurcates to periodic, quasiperiodic, and steady state (fixed point) as the system moves beyond the onset. These patterns have been obtained in our direct numerical simulations (DNS) and a low-dimensional model derived using the energetic modes of DNS. The origin of the patterns including chaotic attractors is explained using bifurcation diagrams.

term of the Navier-Stokes equation plays an important role, and it generates vertical vorticity resulting in three-dimensional patterns and the associated secondary oscillatory patterns.⁷⁻⁹ In the present paper, we will study various patterns and chaos for zero-Prandtl number convection using bifurcation analysis. We use direct numerical simulations (DNS) and a low-dimensional model for this purpose.

Low-Prandtl number fluids, for example, mercury ($P \approx 0.02$), liquid sodium ($P \approx 0.01$), liquid potassium ($P \approx 0.005$), and solar plasma in the convective zone ($P \sim 10^{-8}$) exhibit interesting convective patterns and chaos.¹⁰⁻¹⁵ In the terrestrial experiments performed so far, potassium has the lowest Prandtl number. Note, however, that visualization of flow patterns inside low- P fluids like liquid metal is quite difficult. This difficulty does not arise in numerical simulation, in which we can probe fields at any point of the system. The numerical work of Thual¹⁶ indicates that the properties of low- P convection as $P \rightarrow 0$ are quite close to that of zero- P convection. Therefore, zero- P convection is very useful for understanding the properties of low- P convection. Even though numerical analysis of zero- P convection is quite tricky due to its inherent instabilities near the onset, it provides certain advantages. For $P=0$, the thermal modes are slaved to the velocity modes, hence the number of independent variables are less than those required for low- P analysis. Also, the time steps for the numerical simulations of low- P convection are very small due to the stiffness of the equations,¹⁷ which is not a limitation for zero- P convection.¹⁶ These features led us to investigate zero- P convection in detail for understanding the convective patterns and chaos in low- P fluids.

Thual¹⁶ was one of the first to simulate zero- P convection for free-slip and no-slip boundary conditions. He reported various supercritical oscillatory instabilities, regular and chaotic patterns, etc., in his simulations. The patterns observed by Thual are two-dimensional rolls, periodic and

I. INTRODUCTION

Origin of instabilities, patterns, and chaos in Rayleigh-Bénard convection (RBC) is an interesting problem in fluid dynamics.¹⁻⁶ Prandtl number, P (ratio of kinematic viscosity ν and thermal diffusivity κ) and Rayleigh number, R (ratio of buoyancy and dissipative terms) are the two critical parameters for RBC. Some of the key and difficult problems in this field are related to the onset of convection for zero-Prandtl number and low-Prandtl number fluids. We point out that $P=0$ limit can be achieved by taking $\nu \rightarrow 0$ and $\kappa = \text{finite}$ or $\kappa \rightarrow \infty$ and $\nu = \text{finite}$. In the present study, we assume the latter. Under such conditions, for zero-Prandtl number (zero- P) and low-Prandtl number (low- P) convection, the nonlinear

^{a)}Present address: Computational Fluid Dynamics Team, Scientific and Engineering Computation Group, Centre for Development of Advanced Computing, Pune 411 007, India. Electronic mail: supriyop@cdac.in.

^{b)}Electronic mail: wahi@iitk.ac.in.

^{c)}Electronic mail: mkv@iitk.ac.in.

quasiperiodic rolls, squares, travelling waves, etc., for low- P convection. For low- P fluids, Meneguzzi *et al.*¹⁸ performed numerical simulations for $P = 0.2$ under stress-free boundary conditions and for $P = 0.025$ under no-slip boundary conditions and observed similar patterns. Clever and Busse¹⁹ found travelling wave solutions for low- P convection under no-slip boundary conditions. These observations indicate that zero- P convection contains pertinent features of low- P convection.

Regular and chaotic patterns found in numerical simulations have also been observed in convection experiments on mercury, air, and liquid sodium.^{20–27} Some of the most commonly observed patterns in experiments are stationary, periodic, quasiperiodic, chaotic, and travelling rolls as well as squares (SQ), asymmetric squares (ASQ), and phase locked states. Chaotic rolls have been observed to appear through both period doubling and quasiperiodic routes in some of these experiments.

Convection experiments^{21,22,26,27} and numerical simulations^{16,18,19,29,30} indicate the presence of oscillatory instability of the two-dimensional convective rolls and the resultant stable wavy rolls. Busse and coworkers^{7–9} showed using perturbative analysis that the two-dimensional rolls become unstable due to oscillatory disturbances when the amplitude of the convective motion exceeds a finite critical value. According to Busse,⁷ the condition for the instability takes the form

$$\frac{R_t}{R_c} - 1 \approx 0.310P^2, \quad (1)$$

where R_c is the critical Rayleigh number for the onset of convection, and R_t is the Rayleigh number, where oscillatory instability starts. In addition, the time period of the oscillations measured in the units of d^2/ν (viscous time scale) is independent of P (Eq. (5.2) of Busse⁷). In a related work, Fauve *et al.*³¹ investigated the origin of instabilities in low- P convection using phase dynamical equations and argued that the instability always saturates into travelling waves. In the present paper, we will explore the origin of this oscillatory instability and related flow patterns using numerical simulations and bifurcation theory.

Origin of different convective patterns observed in experiments and numerical simulations can be quite intricate. Each run of a convective simulation takes significantly long time, so it is very difficult to scan the parameter space minutely for deciphering detailed bifurcation scenario. Experiments too have their complexities and limitations. The large number of modes present in simulations and experiments tend to obscure the underlying dynamics. These difficulties are circumvented by a powerful and complementary approach in which the system is analysed using appropriately constructed low-dimensional models. Relatively low computational cost for running low-dimensional models and the ease of construction of the bifurcation diagrams are some of the distinct advantages of these models compared to the experiments and simulations. However, care must be taken to consider all the relevant modes of the system for constructing the low-dimensional models.

Number of active modes near the onset of convection is not very large, so low-dimensional models consisting of these active modes are very useful for analysing this regime. Kumar *et al.*³² showed using a 6-mode model of zero- P convection that the growth of the 2D rolls saturates through the generation of vertical vorticity (wavy nature). Kumar *et al.*³³ observed critical bursting in the above model during the saturation. Pal and Kumar³⁴ explained the mechanism of the selection of the square patterns using a 15-mode model of zero- P RBC. Recently Pal *et al.*¹ constructed a 13-mode model using the energetic modes of DNS, and performed a bifurcation analysis using the model and simulation results. Using the bifurcation diagram, Pal *et al.*¹ could explain the origin of SQ, ASQ, oscillating asymmetric squares (OASQ), relaxation oscillations with an intermediate square regime (SQOR), and three kinds of chaotic attractors. The above patterns were also observed in their DNS. Earlier, Thual¹⁶ had observed SQ and SQOR patterns in his simulations. Jenkins and Proctor³⁵ studied the transition from 2D rolls to square patterns in RBC for different Prandtl numbers using analytical tools. Knobloch³⁶ studied the stability of the SQ patterns using a complementary procedure called the amplitude equations.

A major limitation of the 13-mode model of Pal *et al.*¹ was the absence of wavy rolls near the onset. This limitation is overcome by extending this model to a 27-mode model by incorporating the corresponding dominant modes. In the present paper, we perform a bifurcation analysis of this model and explore the origin of the various convective patterns of zero- P convection with special emphasis on the oscillatory instability and related wavy roll patterns. All the features of the 13-mode model are reproduced in the 27-mode model by construction. We will show in our discussions that the properties of the wavy rolls of the 27-mode model match reasonably well with those observed in experiments and simulations.

The organization of the paper is as follows: In Sec. II, we describe the basic hydrodynamic system considered for the study. The low dimensional model will be derived in Sec. III. Section IV contains the results of the numerical simulations and the low-dimensional model. Various bifurcation diagrams are described in this section. A study of the wavy rolls observed in the low-dimensional model is presented in Sec. V. Section VI contains a brief discussion on the symmetries of our system and the observed patterns. We finally conclude in Sec. VII.

II. GOVERNING EQUATIONS AND DIRECT NUMERICAL SIMULATIONS

In Rayleigh-Bénard convection, a conducting fluid is confined between two conducting plates separated by a distance d and heated from below. The convection in the system is governed by the Navier-Stokes equation along with the heat diffusion equation.² In the zero- P limit, these equations under Boussinesq approximation² take the form^{16,37}

$$\partial_t(\nabla^2 v_3) = \nabla^4 v_3 + R \nabla_H^2 \theta - \hat{\mathbf{e}}_3 \cdot \nabla \times [(\boldsymbol{\omega} \cdot \nabla) \mathbf{v} - (\mathbf{v} \cdot \nabla) \boldsymbol{\omega}], \quad (2)$$

$$\partial_t \omega_3 = \nabla^2 \omega_3 + [(\omega \cdot \nabla) v_3 - (\mathbf{v} \cdot \nabla) \omega_3], \quad (3)$$

$$\nabla^2 \theta = -v_3, \quad (4)$$

$$\nabla \cdot \mathbf{v} = 0, \quad (5)$$

where $\mathbf{v}(x, y, z, t) \equiv (v_1, v_2, v_3)$ is the velocity field, $\theta(x, y, z, t)$ is the deviation in the temperature field from the steady conduction profile, $\omega \equiv (\omega_1, \omega_2, \omega_3) \equiv \nabla \times \mathbf{v}$ is the vorticity field, $\hat{\mathbf{e}}_3$ is the vertically directed unit vector, and $\nabla_H^2 = \partial_{xx} + \partial_{yy}$ is the horizontal Laplacian. The equations have been nondimensionalized using d as the length scale, d^2/ν as the time scale, and $\nu\beta d/\kappa$ as the temperature scale, where ν and κ are the kinematic viscosity and the thermal diffusivity of the fluid, respectively. $\beta = (T_l - T_u)/d$ is the uniform temperature gradient applied across the fluid layer, with T_l and T_u as the constant temperatures of the lower and upper plates, respectively. In the above set of equations, we assume $\kappa \rightarrow \infty$ while ν is finite, such that $P \rightarrow 0$. In the zero-P limit, temperature field $\theta(x, y, z)$ is slaved to the velocity field and is given by Eq. (4). In addition, the velocity field is divergence-less (Eq. (5)) due to the incompressibility condition.²

The nondimensional parameter in the equations is the Rayleigh number $R = \alpha\beta g d^4/\nu\kappa$, where α is the coefficient of volume expansion of the fluid and g is the acceleration due to gravity. In the following discussions, we will also use the reduced Rayleigh number $r = R/R_c$ as a parameter. For our analysis, we consider perfectly conducting boundary conditions for the top and bottom plates along with the free-slip boundary condition for the velocity field. Consequently,

$$v_3 = \partial_z v_1 = \partial_z v_2 = \theta = 0 \quad \text{at} \quad z = 0, 1. \quad (6)$$

We assume periodic boundary conditions along the horizontal directions. These boundary conditions are somewhat idealized, however they help us simplify the computations because of the application of the Fourier basis functions (sin and cos functions). For example, the velocity field can be expressed as

$$\begin{aligned} v_1 &= \sum_{l,m,n} U_{lmn} e^{-ilkx} e^{-imky} \cos(n\pi z), \\ v_2 &= \sum_{l,m,n} V_{lmn} e^{-ilkx} e^{-imky} \cos(n\pi z), \\ v_3 &= \sum_{l,m,n} W_{lmn} e^{-ilkx} e^{-imky} \sin(n\pi z), \end{aligned} \quad (7)$$

where U_{lmn} , V_{lmn} , and W_{lmn} are the Fourier amplitudes corresponding to v_1 , v_2 , and v_3 , respectively, with the three subscripts (l , m , n) indicating the wavenumber components along the x , y , and z directions, respectively, and $k = \pi/\sqrt{2}$.²

Equations (2)–(5) are numerically solved using DNS under the above boundary conditions (Eq. (6)) for $0.98 \leq r \leq 1.25$. DNS were performed using a pseudo-spectral code,³⁸ which was validated against the simulations of Thual.¹⁶ This code reproduces the Nusselt numbers and various convective patterns observed by Thual¹⁶ in his free-slip RBC runs. We simulate the system in a box with aspect ratio $\Gamma_x = 2\sqrt{2}$ and $\Gamma_y = 2\sqrt{2}$.² Grid resolutions, $32 \times 32 \times 32$,

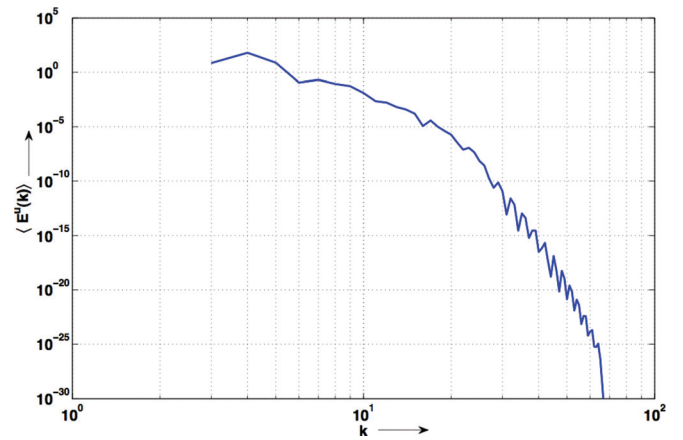


FIG. 1. (Color online) Fully resolved kinetic energy spectrum for $r = 1.1$ and $P = 0$ obtained from DNS on $64 \times 64 \times 64$ grid.

$64 \times 64 \times 64$, have been used for the simulations. Our runs are dealiased using 2/3 rule. We use fourth-order Runge-Kutta scheme (RK4) for time advancement. The time increment dt is determined using the Courant-Friedrichs-Lewy (CFL) condition ($dt = \Delta x/\sqrt{20E^u}$, where Δx is the grid size and E^u is the total kinetic energy). All our simulations are well resolved as evident from a typical kinetic energy spectrum shown in Fig. 1 for $r = 1.1$ on 64^3 grid. The spectrum shows prominent inertial and dissipation regimes. Each DNS run was carried out till the system reaches a statistically steady state.

We perform around 200 simulation runs for $0.98 \leq r \leq 1.25$. The runs provide an approximate picture of the bifurcations associated with the system. However, these many simulations are not sufficient for obtaining a detailed bifurcation diagram. Also the large number of modes present in the DNS obscures the dynamics of the system. Moreover, DNS runs are computationally very expensive in terms of computer time and memory. Therefore, for creating a complete bifurcation diagram for the above range of r , we construct a low-dimensional model, which will be described in Sec. III.

III. LOW-DIMENSIONAL MODEL

We identify Fourier modes that have significant amount of energy in the DNS runs. These modes individually carry 1% or more of the total energy. We attempt to incorporate as many triadic interactions as possible between these modes and find that 27 modes are ideal. We choose these 27 modes and create a low-dimensional model. It is worthwhile to mention the rationale behind the choice of 27-mode model over the 13-mode model of Pal *et al.*¹ The 13-mode model was successful in explaining different bifurcation scenario observed in DNS. However, we observed certain patterns in DNS (for example, “wavy roll pattern,” which will be described later) that the 13-mode model does not capture. In order to reproduce “wavy rolls” and associated patterns, it is necessary to consider interactions between modes outside the realm of 13-mode model. The next minimal model involves 27 modes that capture the DNS results satisfactorily. The modes of the model are shown in Fig. 2 and they account for approximately 98% of the total energy. The triangles represent the interacting triads. Note that only some

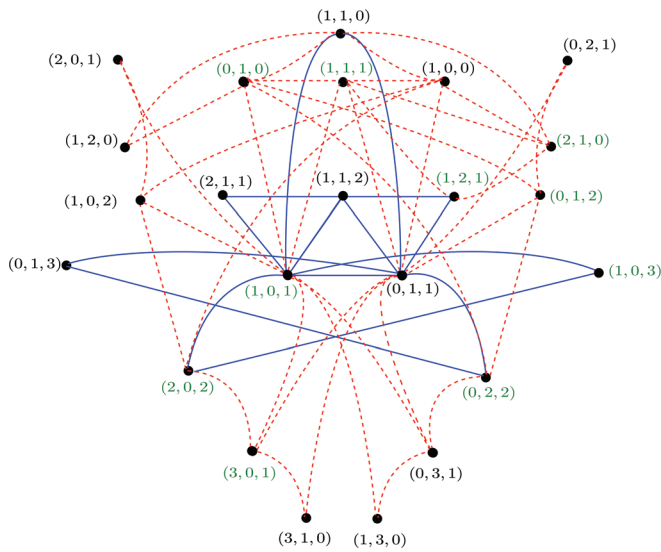


FIG. 2. (Color online) The interacting modes of the 27-mode model. Interactions corresponding to the 13-mode model are shown in blue solid curves, whereas new interactions unique to 27-mode model are shown in red dashed curves. The modes in grey (green online) are active in the wavy roll flow patterns. Note that the modes (1, 1, 1), (1, 1, 2), (1, 2, 1) and (2, 1, 1) contain both the W and Z terms.

of the interacting triads of the model have been shown in the figure. Care has been taken to include sufficient number of modes so that the model reproduces many features found in experiments and simulations. The vertical velocity field (v_3) and vertical vorticity field (ω_3) in terms of the chosen modes are

$$\begin{aligned}
 v_3 = & 2W_{101}(t) \cos(kx) \sin(\pi z) + 2W_{011}(t) \cos(ky) \sin(\pi z) \\
 & + 2W_{202}(t) \cos(2kx) \sin(2\pi z) \\
 & + 2W_{022}(t) \cos(2ky) \sin(2\pi z) \\
 & + 2W_{103}(t) \cos(kx) \sin(3\pi z) + 2W_{013}(t) \cos(ky) \sin(3\pi z) \\
 & + 2W_{301}(t) \cos(3kx) \sin(\pi z) + 2W_{031}(t) \cos(3ky) \sin(\pi z) \\
 & + 4W_{121}(t) \cos(kx) \cos(2ky) \sin(\pi z) \\
 & + 4W_{211}(t) \cos(2kx) \cos(ky) \sin(\pi z) \\
 & + 4W_{112}(t) \cos(kx) \cos(ky) \sin(2\pi z) \\
 & + 4W_{111}(t) \sin(kx) \sin(ky) \sin(\pi z), \tag{8}
 \end{aligned}$$

$$\begin{aligned}
 \omega_3 = & 2Z_{100}(t) \cos(kx) + 2Z_{010}(t) \cos(ky) \\
 & + 4Z_{110}(t) \sin(kx) \sin(ky) \\
 & + 4Z_{112}(t) \sin(kx) \sin(ky) \cos(2\pi z) \\
 & + 4Z_{310}(t) \sin(3kx) \sin(ky) + 4Z_{130}(t) \sin(kx) \sin(3ky) \\
 & + 4Z_{120}(t) \cos(kx) \cos(2ky) + 4Z_{210}(t) \cos(2kx) \cos(ky) \\
 & + 2Z_{102}(t) \cos(kx) \cos(2\pi z) + 2Z_{012}(t) \cos(ky) \cos(2\pi z) \\
 & + 2Z_{201}(t) \cos(2kx) \cos(\pi z) + 2Z_{021}(t) \cos(2ky) \cos(\pi z) \\
 & + 4Z_{111}(t) \cos(kx) \cos(ky) \cos(\pi z) \\
 & + 4Z_{121}(t) \sin(kx) \sin(2ky) \cos(\pi z) \\
 & + 4Z_{211}(t) \sin(2kx) \sin(ky) \cos(\pi z), \tag{9}
 \end{aligned}$$

where $k = \pi/\sqrt{2}$ (Ref. 2) and W_{lmn} and Z_{lmn} are the Fourier amplitudes of the vertical velocity and vertical vorticity modes, respectively. The modes (1, 0, 1) and (0, 1, 1) are the

most important modes of our model and they represent the rolls along y and x directions, respectively. For the square pattern, the most important participating triad is $\{(1,0,1), (0,1,1), (1,1,2)\}$. In the above set of modes, we have taken only the real part of the Fourier expansion [Eq. (7)] in a specific manner to minimize the number of variables for the low-dimensional model. Strictly speaking these modes do not satisfy the periodic boundary conditions. The low-dimensional system supports standing waves but no travelling waves.

The horizontal components of the velocity field can be computed using the incompressibility condition of the velocity field (Eq. (5)), and the temperature field θ can be computed using Eq. (4). A Galerkin projection of the RBC equations (2) and (3) on the above modes provides a set of 27 coupled first-order ordinary differential equations (ODEs) for the amplitudes of the above Fourier modes. We perform a detailed bifurcation analysis on this 27-mode model. We will describe the bifurcation diagrams in the subsequent sections.

Our 27-mode model is a superset of the 13-mode model of Pal *et al.*¹ The nonlinear interactions of the 13-mode model are indicated by blue curves in Fig. 2. Additional interactions induced by the new modes of the 27-mode model are represented by red curves in the figure. We note at this point that the size of an appropriate low-dimensional model does not increase in steps of one. For example, inclusion of the mode (1, 1, 1) immediately requires inclusion of (0, 1, 0) and (1, 0, 0), which are produced by nonlinear interactions with primary modes (1, 0, 1) and (0, 1, 1). Introduction of these modes with the other modes of the 13-mode model of Pal *et al.*¹ generates several secondary and tertiary modes. The modes which have the maximum interactions with each other have been retained.

As discussed earlier, primary motivation for the 27-mode model is to be able to generate wavy rolls. The triads $\{(0, 1, 0), (1, 0, 1), (1, 1, 1)\}$ and $\{(1, 0, 0), (0, 1, 1), (1, 1, 1)\}$ play a critical role in inducing wavy rolls along the y and x axes, respectively. In the present paper, we will investigate the dynamics of these wavy rolls in RBC using numerical simulations and the 27-mode model.

We numerically solve the 27-mode model by employing accurate ODE solvers of MATLAB. These simulations reveal a variety of convective patterns: SQ, ASQ, OASQ, relaxation oscillations with an SQOR or alternating rolls, wavy rolls, chaotic squares (SQCH), etc. We have illustrated three snapshots each of OASQ in Fig. 3, SQOR in Fig. 4, and wavy rolls in Fig. 5. For dynamics of these patterns as well as other patterns mentioned in this paper, refer to the accompanying videos available online.³⁹ Note that all the above patterns were also found in our DNS. Earlier, Thual¹⁶ in his DNS of zero-P convection had shown the existence of SQ, SQOR, oscillatory quasi-hexagons (SQOS), SQCH, and chaotic quasi-hexagon (HXCH). Thual observed the oscillatory and chaotic quasi-hexagons for Rayleigh numbers beyond the range investigated in this paper.

We investigate the origin of various convective flow patterns from the bifurcation diagrams generated using the low dimensional model. To generate the bifurcation diagram, we start first with the fixed points of the system. We compute

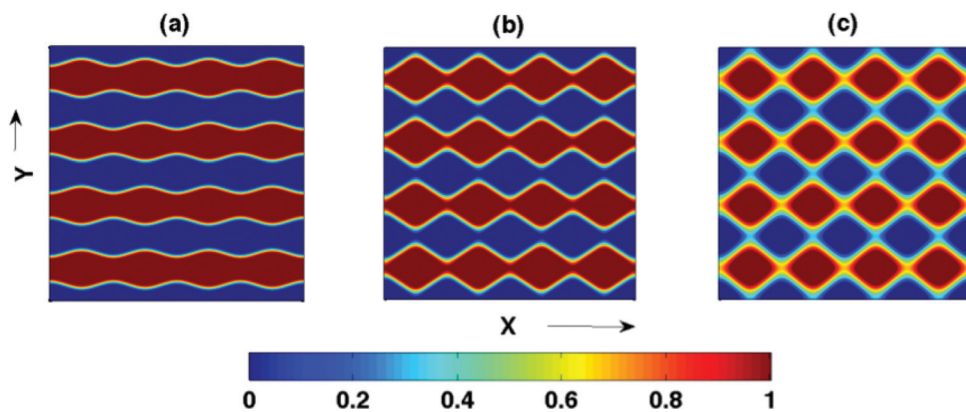


FIG. 3. (Color online) OASQ pattern in the mid-plane of the convection box in zero-P RBC plotted on a square of size $8\sqrt{2} \times 8\sqrt{2}$. The pattern is obtained from the 27-mode model at $r=1.1$ by plotting the temperature contours. Snapshots at: (a) $t=0$, (b) $t=T/4$, and (c) $t=T/2$, where T is the time period of oscillation.

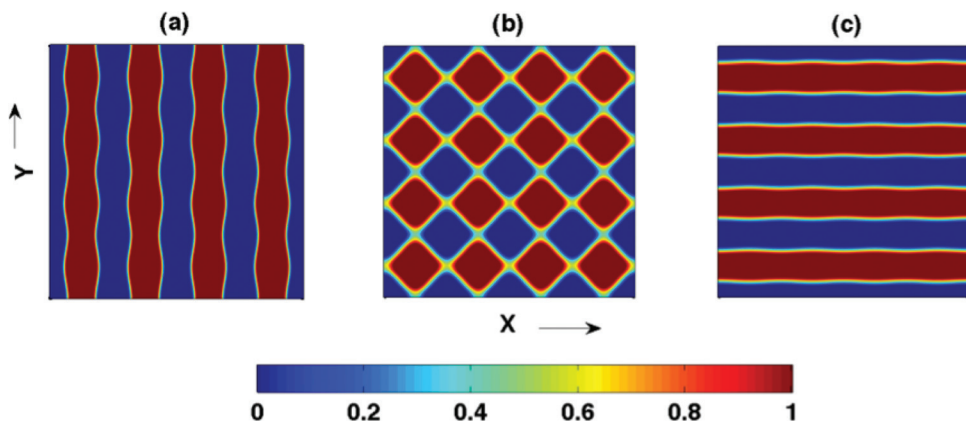


FIG. 4. (Color online) Alternating rolls or relaxation oscillations with an SQOR pattern plotted on a square of size $8\sqrt{2} \times 8\sqrt{2}$ at $r=1.05$. The pattern is obtained from the 27-mode model by plotting the temperature contours. Snapshots at: (a) $t=0$, (b) $t=T/4$, and (c) $t=T/2$.

the fixed points using the Newton-Raphson method for a given r , and these fixed points are subsequently continued using a fixed arc-length based continuation scheme for the neighbouring r values.^{40,41} The stability of the fixed points are ascertained through an eigenvalue analysis of the Jacobian. New branches of fixed points and limit cycles are born when the eigenvalue(s) become zero (pitchfork) and purely imaginary (Hopf), respectively. This process is continued on the new branch. For aperiodic and chaotic solutions, we resort to numerical integration and report the extrema of the important modes. We use our own MATLAB code as well as MATCONT (Ref. 42) for the analysis. The use of continuation in conjugation with a Newton-Raphson scheme for fixed points (steady patterns) and limit cycles (periodic patterns)

provides an added advantage in the computational costs as opposed to DNS. They also allow us to locate the origin of the various flow patterns as a bifurcation point of the low-dimensional system.

IV. BIFURCATION ANALYSIS USING MODEL AND SIMULATION RESULTS

In the present section, we numerically solve Eqs. (2)–(5) using DNS and the 27-mode model in the range $0.98 \leq r \leq 1.25$. This range of r values is near the onset of convection. We will present the bifurcation diagrams associated with the different attractors using the low-dimensional model followed by a detailed comparison of the model results with those obtained from DNS.

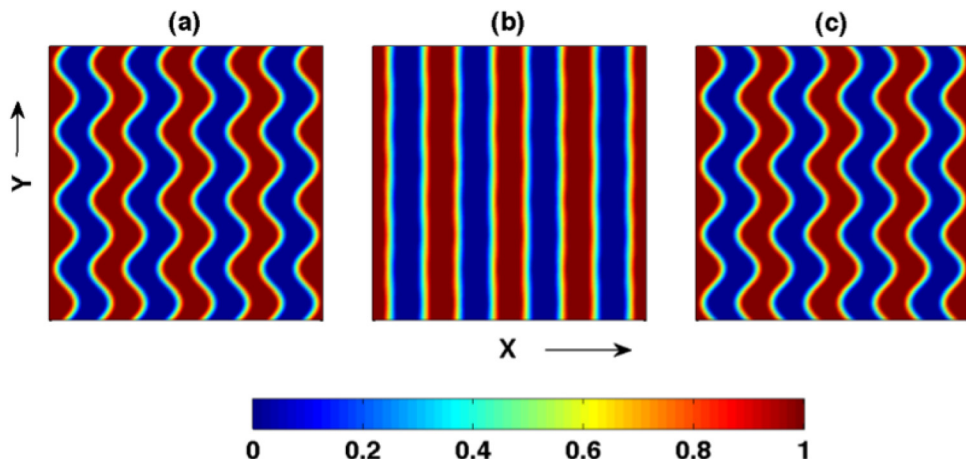


FIG. 5. (Color online) Wavy roll pattern observed in the 27-mode model at $r=1.15$ by plotting the temperature contours on a square of size $8\sqrt{2} \times 8\sqrt{2}$. Snapshots at: (a) $t=0$, (b) $t=T/4$, and (c) $t=T/2$.

A. Fixed points of the system

Fixed points of a dynamical system and their bifurcations provide important clues about the system dynamics. Therefore, we start our analysis by locating all the fixed points of the 27-mode model. In Fig. 6, we display the fixed points of $|W_{101}|$ as a function of r . For $r < 1$, the only stable fixed point of the system is $W_{101} = W_{011} = 0$, which corresponds to the pure conduction state (cyan curve). At $r = 1$, the conduction state loses stability and pure roll solutions (purple curve of Fig. 6) are born. The fixed points at $r = 1$ have certain peculiar properties. Pure roll solutions are exact solutions of the nonlinear Equations (2)–(4) only for zero-P convection. Specifically, we can have infinitely many 2D roll fixed point solutions with mode amplitudes $0 < W_{101} < 13.46$, $W_{011} = 0$ and vice versa. At any one of these fixed points, the stability matrix shows one zero eigenvalue (rest of the eigenvalues are all negative). The fixed point is, therefore, not attracting, yet it is stable. Four unstable branches of symmetric square solutions (dotted black curve of Fig. 6) satisfying $|W_{101}| = |W_{011}|$ are also born at $r = 1$. Note that the stability matrix at the origin (CB1) has double zero eigenvalues.

The pure roll solutions of the $r = 1$ line become unstable through another bifurcation at CB2 $\{(W_{101} \simeq \pm 13.44, W_{011} = 0); (W_{101} = 0, W_{011} \simeq \pm 13.44)\}$, which is represented by a red dot at $r = 1$. The stability matrix at CB2 has a zero eigenvalue and a purely imaginary pair ($\lambda_c = (0, \pm i\omega)$ with $\omega \approx 14.2$). As a consequence of the complex eigenvalues of CB2, periodic solutions are born for $r > 1$ from this point, and the 2D rolls lose their stability (chained purple line of Fig. 6). These periodic solutions are also unstable akin to the symmetric square fixed points associated with CB1. We will show later that the wavy rolls are associated with CB2.

The unstable roll solutions which persist at $r = 1$ with amplitudes greater than 13.44 subsequently undergo yet another bifurcation at CB3 $\{(W_{101} = \pm 26.94, W_{011} = 0)$;

$(W_{101} = 0, W_{011} = \pm 26.94)\}$, which is represented as a green square on the $r = 1$ line (see Fig. 6). The stability matrix at CB3 has two zero eigenvalues ($\lambda_c = 0, 0$) along with a pair of complex eigenvalues with positive real parts. Rest of the eigenvalues are all negative or complex with negative real parts. Consequently, unstable asymmetric square solutions with $|W_{101}| \neq |W_{011}|$ (dotted blue curves) are born. This bifurcation is also present in the 13-mode model,¹ and the attractors associated with this bifurcation in the 13-mode model carry over to the 27-mode model as well.

For low-P convection, Mishra *et al.*¹⁷ have earlier observed that the 2D rolls undergo a pitchfork bifurcation followed by a Hopf. In the limiting case of zero-P, the Hopf bifurcation point merges with the pitchfork bifurcation point at $r = 1$, and the critical eigenvalues at this bifurcation point are $(0, 0)$ (CB3). With an increase in r , the double zero eigenvalues split into unstable complex conjugate pair giving rise to a scenario very similar to the Takens-Bogdanov bifurcation.^{43,44}

There are 13 unstable fixed points for $r > 1$ for the 27-mode model: one corresponding to the pure conduction state, four satisfying $|W_{101}| = |W_{011}|$ (SQ), and the remaining eight satisfying $|W_{101}| \neq |W_{011}|$ (ASQ). After two successive inverse Hopf bifurcations, to be described later, the unstable ASQ fixed points become stable. These stable fixed points are shown by the solid blue curves in Fig. 6. Subsequently at $r \approx 1.1690$, these stable ASQs merge (via a pitchfork bifurcation) with the symmetric square solution that originate from CB1 and stabilize them (solid black curve in Fig. 6). Note that there is a small difference in the values of r corresponding to the stabilization of the ASQ solutions and SQ solutions for the 13-mode model and the 27-mode model. In the following discussions, we will describe the bifurcation diagrams including limit cycles, chaotic attractors, etc.

Bifurcation diagrams of the 27-mode model are quite complex. They include six different types of chaotic attractors, various types of fixed points, and periodic solutions.

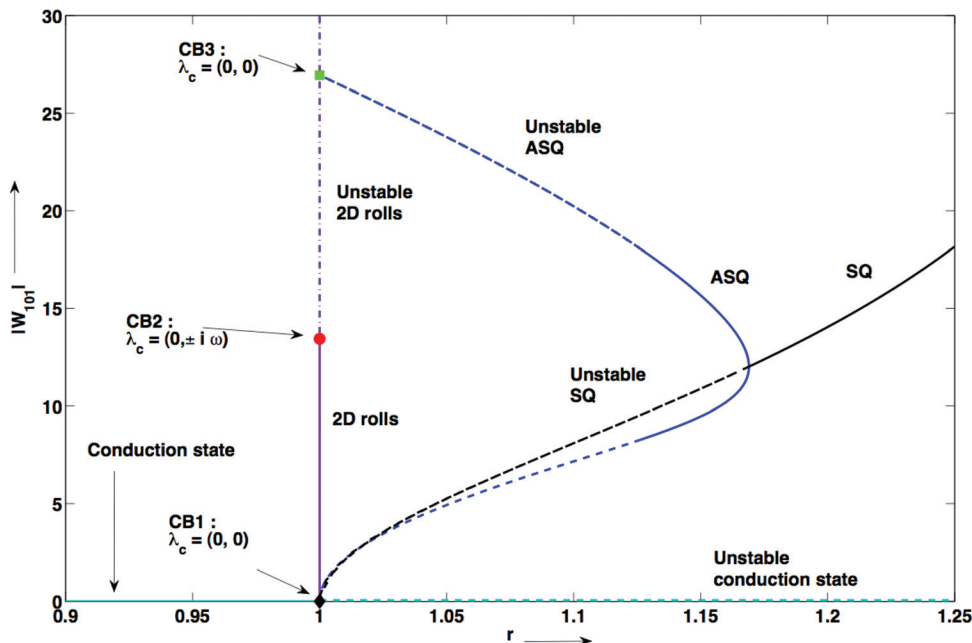


FIG. 6. (Color online) Bifurcation diagram on the $|W_{101}|$ - r plane exhibiting the fixed points only. Solid and dashed curves represent the stable and unstable fixed points, respectively. Black, blue, and cyan curves represent stationary SQ, ASQ, and conduction state, respectively. Solid purple line parallel to the $|W_{101}|$ axis represents the 2D roll solutions and chained purple line represents unstable 2D rolls. CB1 (black diamond), CB2 (red dot), and CB3 (green square) are the bifurcation points on the $r = 1$ plane. The critical eigenvalues at CB1, CB2, and CB3 are denoted by λ_c in the figure. The bifurcation scenario on the $|W_{011}|$ - r plane is also exactly similar.

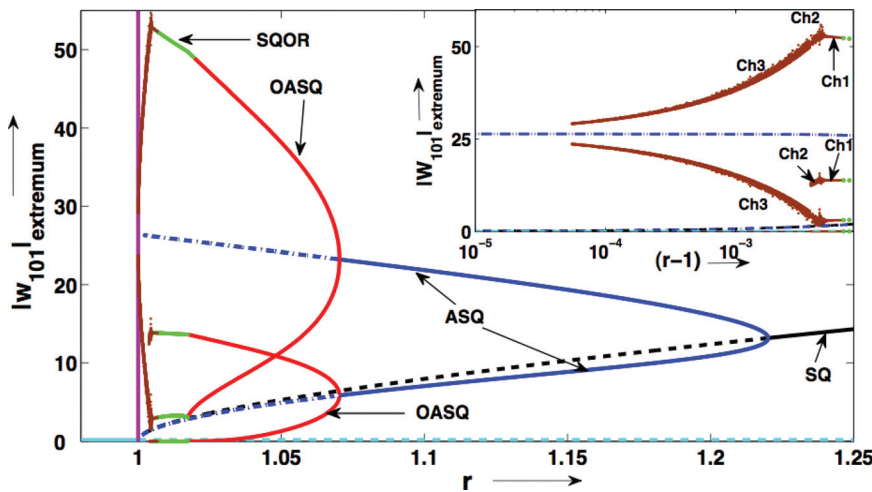


FIG. 7. (Color online) Bifurcation diagram Bif-13M of the 13-mode model for $0.98 \leq r \leq 1.25$ adapted from Pal *et al.*¹ The stable branches corresponding to SQ and ASQ are represented by solid black and blue lines, respectively. Red, green, and brown lines represent the extrema of OASQ, SQOR, and chaotic solutions, respectively. A zoomed view of the bifurcation diagram for the chaotic regime is shown in the inset. Branches corresponding to the unstable fixed points are represented by dashed lines. Cyan line represents the conduction state.

The model also has multiple coexisting attractors for a given value of r . To disentangle its complexity, we present the bifurcation diagrams as four separate diagrams, “Bif-13M,” “Bif-A,” “Bif-B,” and “Bif-C,” that highlight different features of the dynamics. First, we draw the bifurcation diagram “Bif-13M” associated with the 13-mode model,¹ which is a subset of the 27-mode model. Later, we will contrast the bifurcation diagram of the 27-mode model (denoted by “Bif-A”) with the diagram of the 13-mode model.

B. Bifurcation diagram of the 13-mode model

As illustrated in Fig. 2, the 13-mode model is a subset of the 27-mode model. If we force only the modes of the 13-mode model to be nonzero, and others to be zero, naturally the bifurcation diagram corresponding to the 13-mode model is reproduced. Pal *et al.*¹ contain a detailed discussion on this diagram and the associated flow patterns (both from DNS and the model). Here, we only provide a brief description.

The bifurcation diagram for the 13-mode model is illustrated in Fig. 7 in which we plot $|W_{101}|_{\text{extremum}}$ as a function of r . For zero-P convection, chaos is observed at the onset itself. Therefore, Pal *et al.*¹ start their analysis at $r = 1.4$, where symmetric square (SQ) patterns are observed. These states are represented by the solid black curve of Fig. 7 (here the diagram is shown only for $r \leq 1.25$). At around $r \approx 1.2201$, SQ branches bifurcate to ASQ solutions through a supercritical pitchfork bifurcation. The solid blue curves of Fig. 7 correspond to ASQ patterns. The ASQ branches bifurcate to OASQ solutions (the solid red curves) through a Hopf bifurcation. The limit cycles thus generated grow in size and touch the saddles (dashed line of the SQ branch) to create a very narrow window of homoclinic chaos. After this, the system again becomes periodic (SQOR) with the merger of the limit cycles. The SQOR patterns transform to a chaotic attractor *Ch1* through a homoclinic bifurcation. *Ch1* turns to *Ch2* and subsequently to *Ch3* through “crisis.” Pal *et al.*¹ observed these patterns in both model and DNS. Earlier, Thual¹⁶ had observed SQ, ASQ, and SQOR patterns in his DNS runs.

In the subsequent subsections, we will describe the bifurcation scenario for the 27-mode model.

C. Bifurcation diagram Bif-A of the 27-mode model

The square pattern described above is also observed in the 27-mode model. However, for SQ in the 27-mode model, 12 modes $W_{111}, Z_{110}, Z_{112}, Z_{100}, Z_{010}, Z_{111}, Z_{210}, Z_{120}, Z_{201}, Z_{021}, Z_{102},$ and Z_{012} still remain zero. When we continue the SQ branch of the 27-mode model, we obtain a new bifurcation diagram called “Bif-A” shown in Fig. 8. The bifurcation diagram Bif-A is qualitatively similar to Bif-13M except in a narrow window of $1.116 \leq r \leq 1.128$, where additional bifurcations are observed. The ASQ branch of solutions in Bif-A have 17 active modes. Remaining ten modes $W_{111}, Z_{100}, Z_{010}, Z_{111}, Z_{210}, Z_{120}, Z_{201}, Z_{021}, Z_{102},$ and Z_{012} remain zero. It is interesting to note that the two symmetric (in $x - y$) and zero modes of the SQ branch, Z_{110} and Z_{112} , become active for the ASQ branch due to the symmetry breaking.

The new features of Bif-A are as follows. At $r = 1.1260$, the ASQ branch undergoes a supercritical Hopf bifurcation (H1, see Fig. 9) resulting in a time-periodic convective flow as illustrated in Figs. 10(a) and 10(b), where we show a projection of the limit cycle obtained from the DNS and the model on the $W_{111} - Z_{010}$ plane. The subspace of the ASQ solution is spanned by 17 non-zero modes. The H1 Hopf bifurcation excites new modes perpendicular to that subspace. All the 27 modes are now active for these periodic flow patterns. Therefore, the limit cycle lies on a bigger subspace than ASQ.

As r is reduced further, at $r = 1.1257$ a new frequency incommensurate with the original frequency is born through a Neimark-Sacker bifurcation (NS1), and the limit cycle becomes unstable. Here, a pair of imaginary Floquet multipliers cross the unit circle outwards as illustrated in Fig. 11(a). The phase space trajectory of the system on the $W_{111} - Z_{010}$ plane is therefore quasiperiodic as demonstrated in Figs. 10(c) and 10(d) for the DNS and the model, respectively.

On further reduction of r , at $r = 1.1226$, another Hopf bifurcation (H2) takes place on the unstable ASQ branch. The limit cycle born from H2 lies on the same subspace as that of ASQ. However, the limit cycle is unstable. At $r = 1.1181$, this limit cycle becomes stable via an inverse Neimark-Sacker bifurcation (NS2), wherein the unstable Floquet multiplier pair enters the unit circle as evident in Fig.

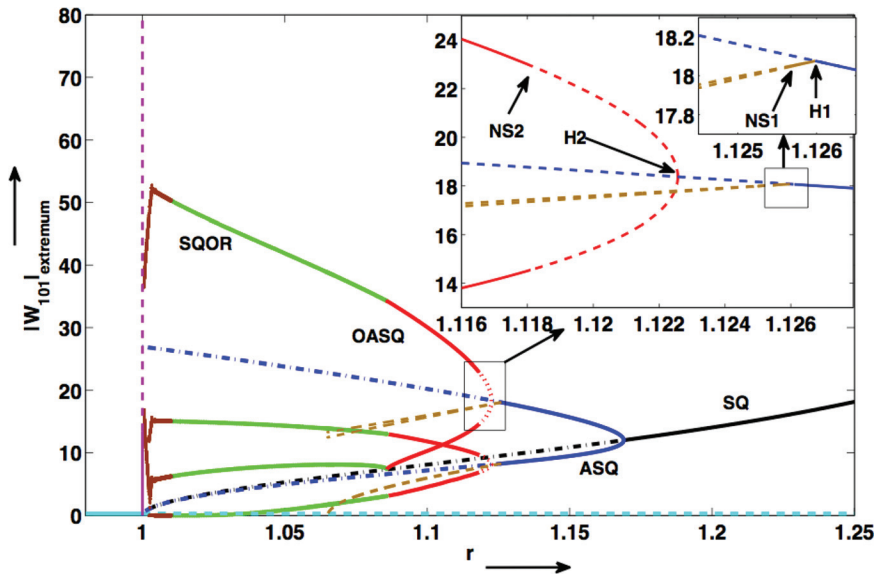


FIG. 8. (Color online) Bifurcation diagram Bif-A of the 27-mode model with the same colour convention as Bif-13M shown in Fig. 7. This diagram is qualitatively similar to Bif-13M. New features of Bif-A are the H1, NS1, H2, and NS2 bifurcations shown in the boxed region ($1.116 < r < 1.128$), whose zoomed view is shown in the inset.

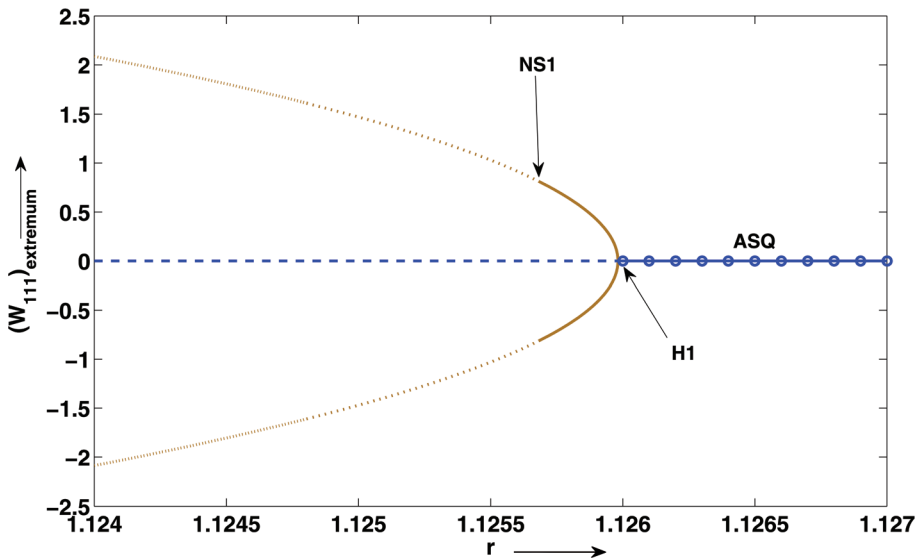


FIG. 9. (Color online) Plot of $(W_{111})_{\text{extremum}}$ vs. r near the first Hopf bifurcation (H1) of the ASQ (blue solid line with circles) branch. The solid brown curve represents the limit cycles generated after the first Hopf (H1).

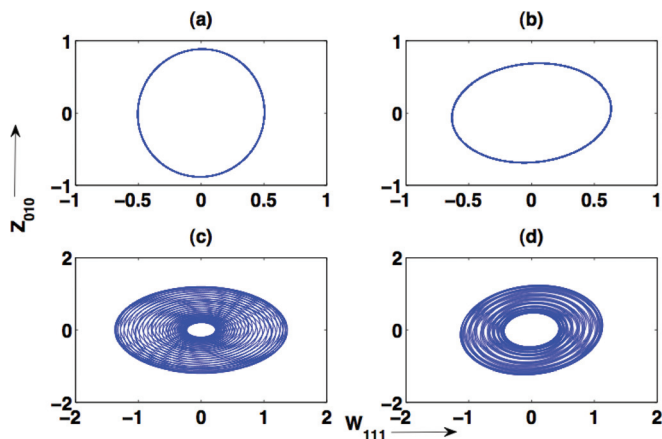


FIG. 10. (Color online) Projection of the phase space on the $W_{111} - Z_{010}$ plane. The limit cycles born through H1 in (a) DNS at $r = 1.138$ and (b) model at $r = 1.1258$. Quasiperiodic attractor born through NS1 in (c) DNS at $r = 1.131$ and (d) model at $r = 1.1245$.

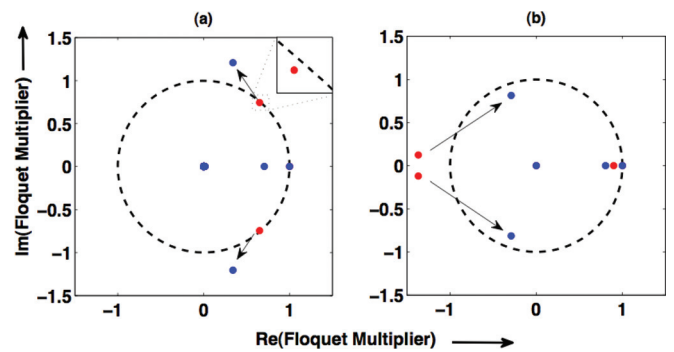


FIG. 11. (Color online) Movement (indicated by the arrows) of Floquet multipliers in the complex plane during NS1 and NS2 bifurcations. (a) At NS1, a pair of complex Floquet multipliers move out of the unit circle (red dots changing to blue). (b) At NS2, a pair of complex Floquet multipliers enters the unit circle (red dots again becoming blue).

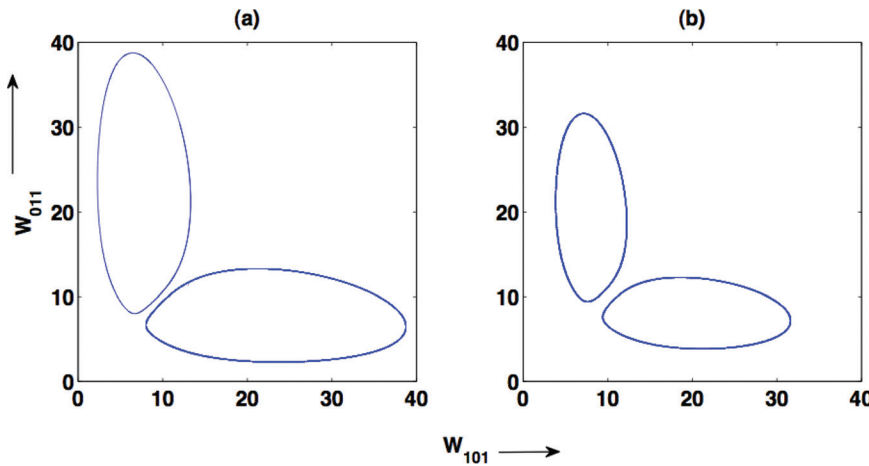


FIG. 12. (Color online) Projections of the two coexisting OASQ solutions on the $W_{101} - W_{011}$ plane just after the NS2 bifurcation point: (a) in DNS at $r=1.0768$ and (b) in the model at $r=1.095$.

11(b). The resulting stable limit cycle is the OASQ solution of the 13-mode model. Figure 12 shows a projection of the limit cycle corresponding to the OASQ solution obtained from the DNS and the model on the $W_{101} - W_{011}$ plane. The quasiperiodic solutions exist only in the range $r = 1.1181 - 1.1257$, i.e., between NS1 and NS2 and disappears after NS2. Note that the attractors between H1 and NS2 contain all the 27 modes, but beyond NS2 the ten modes $W_{111}, Z_{100}, Z_{010}, Z_{111}, Z_{210}, Z_{120}, Z_{021}, Z_{102},$ and Z_{012} again become zero.

Beyond NS2, the patterns and associated bifurcations from OASQ to SQOR to the chaotic attractors $Ch1, Ch2,$ and $Ch3$ in the decreasing r direction are exactly the same as for Bif-13M. The range of r corresponding to these patterns are approximately $r = 1.086 - 1.1181$ for OASQ, $r = 1.0046 - 1.086$ for SQOR, $r = 1.0034 - 1.0046$ for $Ch1$, $r = 1.0025 - 1.0034$ for $Ch2$ and $r = 1 - 1.0025$ for $Ch3$. Comparison with the 13-mode model indicates that the ranges of r for the above patterns as well as that for SQ and ASQ are different. This is due to the fact that more than 13 modes are active in the present model for Bif-A. The 27-mode model reproduces the ranges of the patterns obtained from DNS more accurately.

The attractors from OASQ to SQOR to the chaotic attractors $Ch1, Ch2,$ and $Ch3$ all lie in the subspace spanned by the 17 active modes of the ASQ solutions. The limit cycle

born after H1 and the quasiperiodic attractor born out of this limit cycle at NS1 are attracting, as a numerical noise on the ASQ subspace lead to these attractors. However, after NS2, which happens after H2 on the ASQ subspace, the limit cycle born out of H2 becomes attracting. So in effect, the limit cycle and the quasiperiodic attractor spanning the 27 dimensional spaces are only attracting between H1 and NS2. $Ch1, Ch2,$ and $Ch3$ remain on the same 17-dimensional subspace as that of ASQ. Note that the modes absent for SQ, ASQ, OASQ, SQOR, $Ch1$ to $Ch3$ flow patterns are active for wavy rolls that will be described in Sec. IV E.

D. Bifurcation diagram Bif-B of the 27-mode model

When we start from an arbitrary initial condition for $r > 1$ near the onset, very often the system tends to another attractor $Ch4$, which differs from $Ch1, Ch2,$ and $Ch3$. The bifurcation diagram “Bif-B” shown in Fig. 13 contains the attractor $Ch4$. The attractor $Ch4$ coexists with the chaotic attractors $Ch1, Ch2, Ch3$ and SQOR for $r = 1 - 1.056$. This feature is illustrated in Fig. 14, where a phase space projection (both from the model and DNS) for two different initial conditions at $r = 1.0342$ yield the SQOR (green curve) and the $Ch4$ (grey trajectory) attractors. Clearly, the trajectories

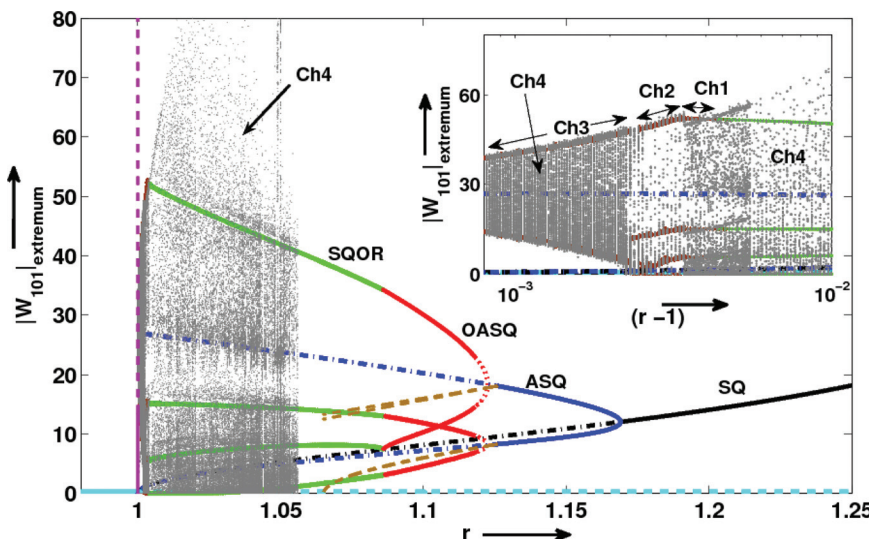


FIG. 13. (Color online) Bifurcation diagram Bif-B with the same colour convention as Bif-13M (Fig. 7). A large chaotic attractor represented by grey dots $Ch4$ is born at CB3. The chaotic attractor $Ch4$ coexists with $Ch1, Ch2, Ch3$ (shown in the inset using brown dots), and SQOR.

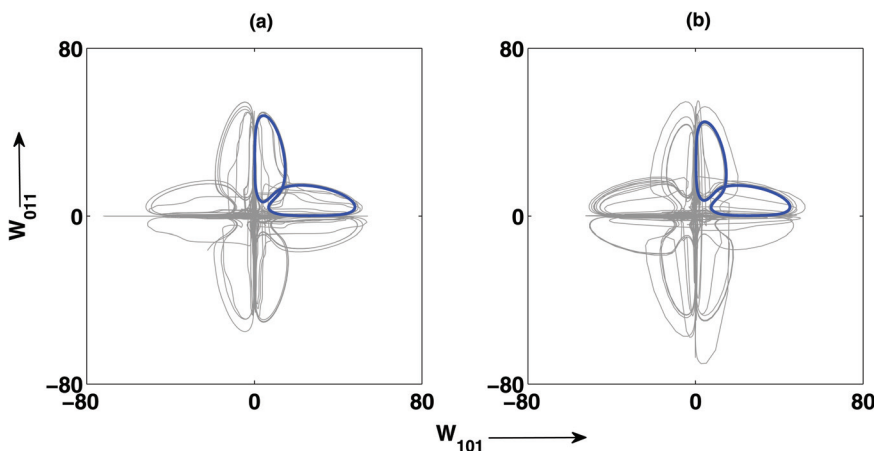


FIG. 14. (Color online) Phase space projection of coexisting SQOR in black (blue online) curve and chaotic attractor *Ch4* in grey curve on the W_{101} - W_{011} plane at $r=1.0342$: (a) obtained from model and (b) obtained from DNS.

of *Ch4* explore all the four quadrants of the W_{101} - W_{011} plane. The qualitative behaviour of the *Ch4* attractor is similar to *Ch2* but its size is larger than *Ch2* (compare with Fig. 5 of Pal et al.¹). Moreover, this attractor lies on a bigger subspace spanned by all the modes of the 27-mode model. *Ch4* is an attracting set, hence any perturbation perpendicular to the 17-dimensional subspace of *Ch1*, *Ch2*, or *Ch3* leads to *Ch4*.

Note that there are two complex pairs of unstable eigenvalues associated with ASQ. The first one carries from CB2, and the second one is due to the splitting of the double zero eigenvalues at CB3 into a complex pair (see Sec. IV A). The *Ch4* attractor is associated with the first pair, while the *Ch3* attractor is related to the second pair. The disappearance of the chaotic attractor *Ch4* is possibly through a boundary crisis,⁴⁵ wherein an unstable periodic solution hits the basin boundaries of *Ch4*. This unstable periodic solution possibly has connections with the unstable periodic solutions originating from the branch point CB2 of Fig. 6.

In Sec. IV E, we will discuss the bifurcations associated with the solutions arising from the branch point CB2, whose flow patterns resemble the wavy rolls.

E. Bifurcation diagram Bif-C of the 27-mode model

The 27-mode model has another class of solutions called “wavy rolls,” which is associated with the CB2 bifurcation point. The bifurcation diagram for the wavy rolls is shown in Fig. 15, which can be best described when we start the analysis from a higher r value to $r=1$. At $r=1.25$, the system shows periodic wavy rolls illustrated in Fig. 5. The attractor for the periodic wavy roll solution for $r=1.15$ is shown in Figs. 16(a) and 16(b) along with its frequency spectrum. The spectrum shows a dominant frequency at $f_1=4.3$. The periodic wavy rolls continue till $r=1.116$, where the system undergoes a Neimark-Sacker bifurcation to generate quasiperiodic wavy rolls, which have been illustrated in Figs. 16(c) and 16(d) for $r=1.10$ along with the power spectrum. The power spectrum shows two incommensurate frequencies f_1 and f_2 with $f_1/f_2 \approx 6.33$. The periodic and quasiperiodic orbits in the bifurcation diagram (Fig. 15) are shown as blue and red curves, respectively.

As r is decreased further, we observe a phase-locked state that subsequently turns into a quasiperiodic state. A phase space projection and the power spectrum of the phase-

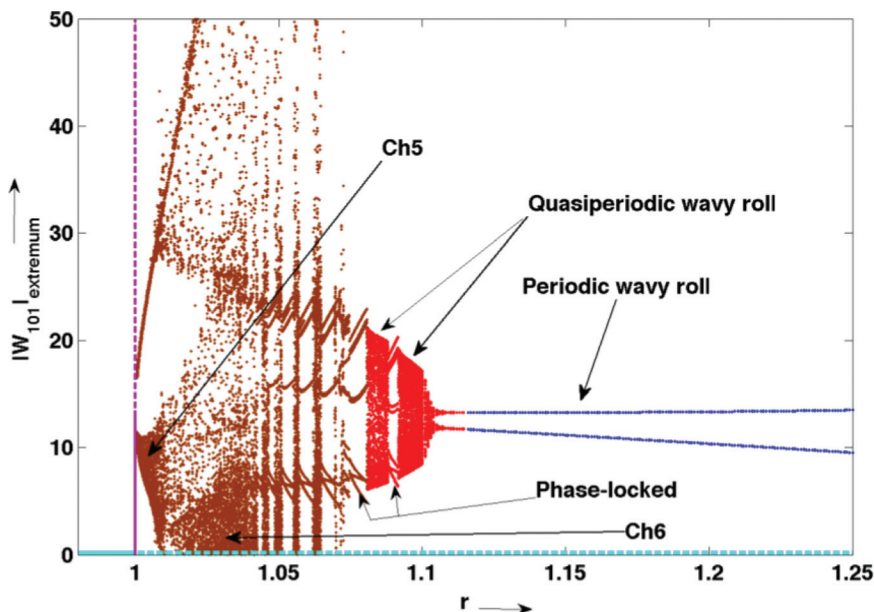


FIG. 15. (Color online) Bifurcation diagram Bif-C of the wavy roll solutions. The blue, red, and brown points represent periodic, quasiperiodic, and chaotic (*Ch5* and *Ch6*) solutions, respectively.

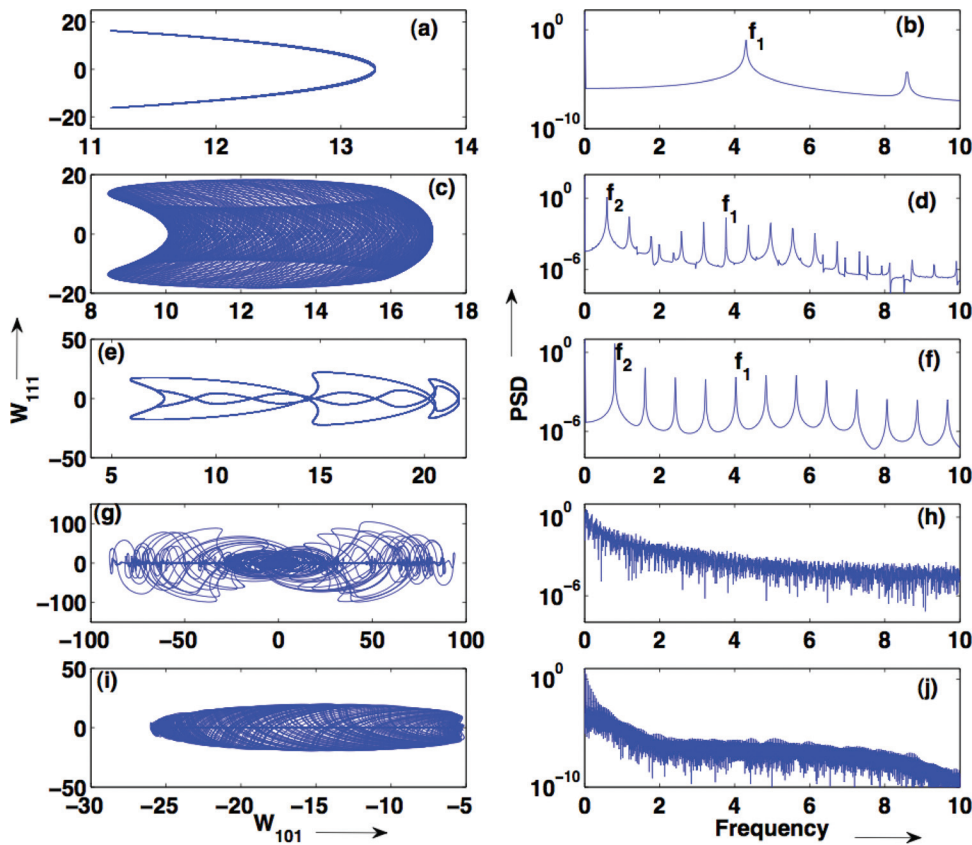


FIG. 16. (Color online) Phase space projections on the W_{101} - W_{111} plane for the wavy rolls and their corresponding power spectra for the W_{101} mode obtained from the model: (a and b) periodic state at $r = 1.15$ ($f_1 = 4.3$); (c and d) quasiperiodic state with $f_1/f_2 \approx 6.33$ at $r = 1.10$; (e and f) frequency locked state with frequency ratio $f_1/f_2 \approx 5$ at $r = 1.078$; (g and h) the chaotic attractor $Ch6$ at $r = 1.05$ with broadband frequency spectrum; (i and j) the chaotic attractor $Ch5$ at $r = 1.005$ with broadband frequency spectrum. Note that there is a symmetric solution for positive W_{101} values.

locked ($r = 1.078$) state are shown in Figs. 16(e) and 16(f), respectively. The banded and the filled regions in the bifurcation diagram Bif-C are the phase-locked and quasiperiodic states, respectively. As r is decreased further, the quasiperiodic attractor bifurcates to a chaotic solution (referred to as $Ch6$) through a quasiperiodic route to chaos in a manner similar to the circle map.⁴⁵ For $r = 1.05$, we exhibit the phase space projection along with the power spectrum in Figs. 16(g) and 16(h). Note that $Ch6$ visits all the four quadrants of the phase space. As r is reduced further, near $r = 1.009$, $Ch6$ separates into two chaotic attractors, referred to as $Ch5$. For $r = 1.005$, the phase space projection of the $Ch5$ attractor is shown in Figs. 16(i) and 16(j) along with its broadband power spectrum. The size of the $Ch5$ attractor reduces as we approach $r = 1$. The attractor $Ch5$ merges with the CB2 bifurcation point at $r = 1$. The above mentioned states have also been observed in DNS. For example, Fig. 17 illustrates periodic, quasiperiodic, and chaotic states obtained in DNS for $r = 1.10$, 1.09, and 1.05, respectively.

When we examine the active modes of Bif-C, we find that only the green coloured modes of Fig. 2 are active for these convective patterns. The attractor therefore lies on a subspace spanned by 12 active modes and is totally different from the ASQ subspace. The bifurcation diagram Bif-C has been generated by setting these modes as non-zero and all other modes as zero. The most important among the active modes of Bif-C are (1, 0, 1), (0, 1, 0), and (1, 1, 1), which are instrumental for the generation of wavy rolls along the y axis. Naturally, the wavy rolls along the x axis will have the complementary set of modes, e.g., (1, 0, 0) instead of (0, 1, 0), etc.

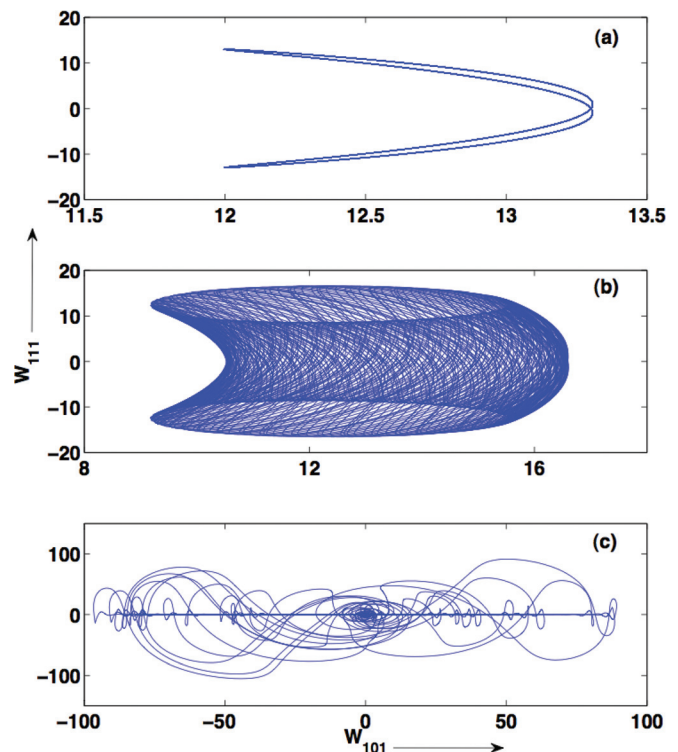


FIG. 17. (Color online) Phase space projections on the W_{101} - W_{111} plane corresponding to the wavy rolls obtained from DNS: (a) the chaotic attractor $Ch6$ at $r = 1.05$; (b) quasiperiodic state at $r = 1.09$; and (c) periodic state at $r = 1.10$.

Note that the above sets of solutions (Bif-A, Bif-B, Bif-C) are observed for different sets of initial conditions. For both DNS and the model, a random initial condition generally produces Bif-B, whose basin of attraction appears to be rather large. If we keep only the green coloured modes of Fig. 2 as nonzero, we obtain Bif-C that corresponds to the wavy rolls. In fact, Bif-C is generated by first constructing a limit cycle for $r = 1.25$ and then continuing the solution for lower r values. The bifurcation diagram Bif-A is generated by starting from the SQ pattern for $r = 1.25$ for which all the modes except $W_{111}, Z_{110}, Z_{112}, Z_{100}, Z_{010}, Z_{111}, Z_{210}, Z_{120}, Z_{201}, Z_{021}, Z_{102},$ and Z_{012} are nonzero. Continuation of the above solution, however, generates ASQ solutions followed by H1, NS1, H2, and NS2 bifurcations where all the 27 modes are present.

Wavy rolls are one of the most studied convective patterns in experiments and numerical simulations. The bifurcation diagram Bif-C provides a clear explanation for the origin of this pattern. In Sec. V, we will provide a quantitative comparison of the bifurcation results related to the wavy rolls with those from the experiments and previous simulations.

V. WAVY ROLLS: A QUANTITATIVE STUDY

In this section, we will analyse time scales of the wavy rolls of Bif-C quantitatively and compare these values with some of the experimental and numerical results. At the bifurcation point CB2, the stability matrix has a pair of complex eigenvalues $(0, \pm i\omega)$ with $\omega \approx 14.2$. As a result, the unstable limit cycle originating from CB2 has a time period around $2\pi/\omega \approx 0.44$ in units of d^2/ν (viscous time scale). Subsequent periodic, quasiperiodic, and chaotic time series have time scales comparable to the above value since their origin is closely connected to CB2. Our preliminary calculations indicate that the time period of oscillations for these patterns are within a factor of 10 from this value for $r = 1-1.25$.

Earlier, Krishnamurti²² observed time-dependent wavy rolls in her convection experiments on mercury ($P \approx 0.02$). She observed multiple peaks with the time period ranging from 0.1 to 1 in the time units of d^2/ν (see Fig. 3 of Krishna-

murti²²). Krishnamurti’s experimental value for the time-scale of the chaotic wavy rolls is in the same range as our theoretical time-scale estimated above. Willis and Dardorff⁴⁶ and Croquette and Williams⁴⁷ reported the time period of the oscillatory rolls using their experimental data for air ($P = 0.7$) to be around 1 in the units of d^2/ν . Using numerical simulations, Lipps²⁹ observed time periods of oscillatory rolls to be around 0.24–0.27 in the units of d^2/κ for $P = 0.7$, which translates to 0.34–0.39 in the units of d^2/ν . Meneguzzi *et al.*¹⁸ found the period of the wavy oscillations to be around 0.065 viscous time units for $P = 0.025$. These results are in general agreement (within an order of magnitude) with our theoretical finding based on the bifurcation analysis. Note that Busse⁷ reported the time period of the oscillatory instability in the units of d^2/ν to be independent of the Prandtl number. Hence, the time-scales are not expected to vary appreciably with the change of the Prandtl number, which is consistent with the results for mercury ($P \approx 0.02$) and air ($P \approx 0.7$). Therefore, a comparison of our results for $P = 0$ with those obtained for finite P is justified.

Oscillatory instabilities and their saturation through critical bursting have been studied by Kumar and coworkers^{32,33} using several low-dimensional models. They show that the growth of the mode W_{101} is saturated by the vorticity mode Z_{010} . The critical bursting is probably due to an attractor bubbling,^{48,49} which needs to be investigated. In Figs. 18(a) and 18(b), we plot the time series of $\langle v_1^2 + v_3^2 \rangle / 2$ (sum of kinetic energy along x and z axes) and $\langle v_2^2 \rangle / 2$ (kinetic energy along y axis) computed from our 27-mode model for $r = 1.05$. These results are in general agreement with the results of Kumar and coworkers.^{32,33} The panel (c) of Fig. 18 shows the time series of the modes $W_{101}, W_{111},$ and Z_{010} that illustrates their growth and subsequent breakdowns (critical bursting). Note that the time-scale of oscillations for the modes W_{111} and Z_{010} is around 0.1, which is in the same range as the theoretical time-scale derived above using the bifurcation analysis.

The above arguments strongly suggest that the origin of the wavy rolls or the oscillatory instabilities are intimately related to the purely imaginary pair of eigenvalues at CB2 and the limit cycles that originate from it.

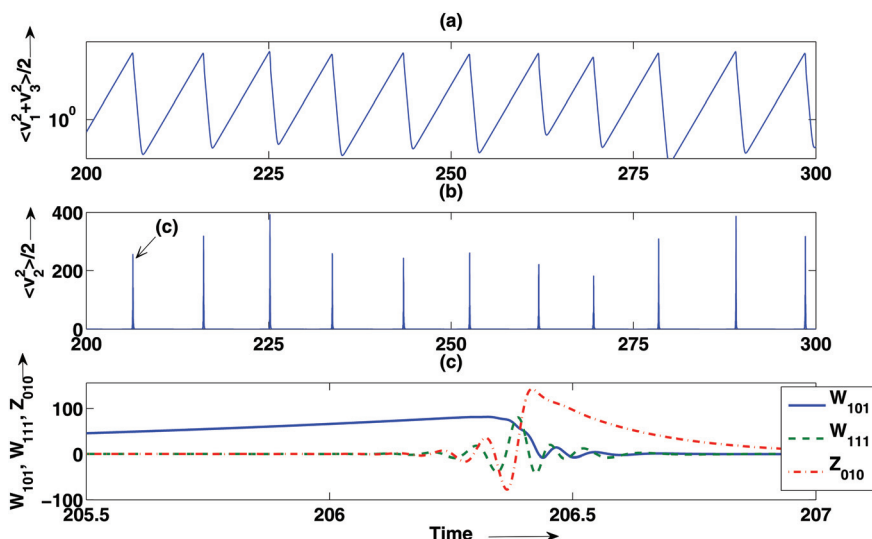


FIG. 18. (Color online) Time series of $\langle v_1^2 + v_3^2 \rangle / 2$ (panel (a)) and $\langle v_2^2 \rangle / 2$ (panel (b)) obtained from the model at $r = 1.05$ illustrating a series of critical bursting. Panel (c) shows the time series of the modes $W_{101}, W_{111},$ and Z_{010} during a critical bursting.

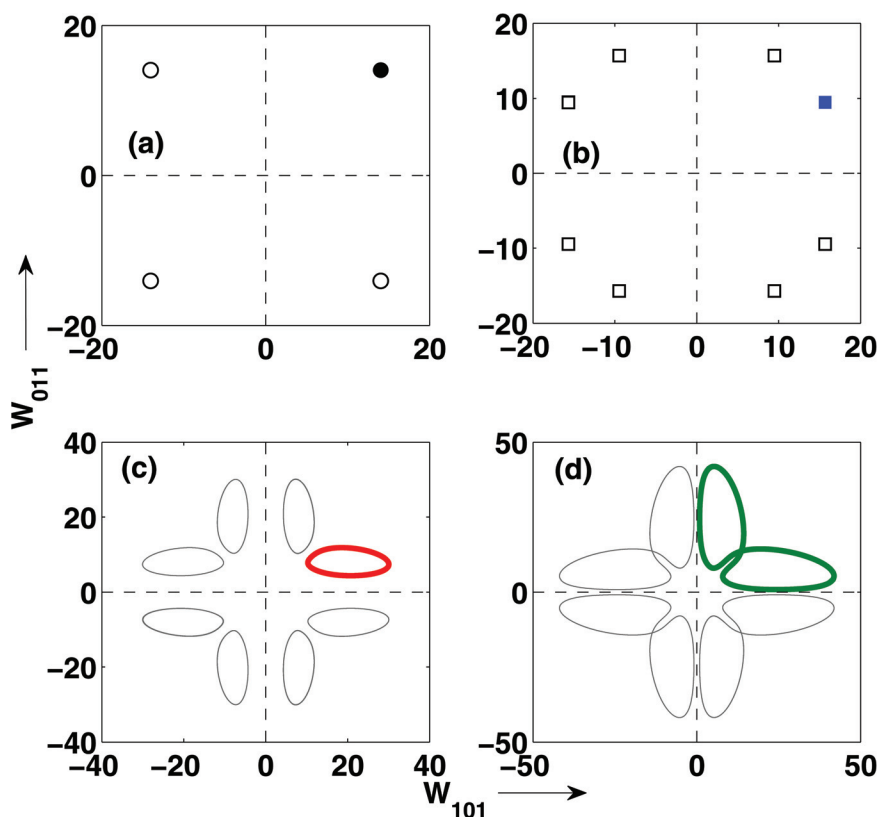


FIG. 19. (Color online) Phase-space projection of the fixed points and the periodic solutions of the 27-mode model on the W_{101} – W_{011} plane. Filled points or coloured thick curves denote the actual solutions, while unfilled points or grey thin curves denote the symmetry related other solutions, which are accessible via other sets of initial conditions. (a) SQ type fixed point solutions at $r=1.2$. Black filled circle denotes the solution on the first quadrant. (b) ASQ type fixed point (blue filled square) solution at $r=1.15$. (c) OASQ periodic solution (red thick curve) at $r=1.1$. (d) SQOR periodic solution (green thick curve) at $r=1.05$.

VI. SYMMETRIES OF THE SYSTEM AND THE OBSERVED PATTERNS

The equations of the 27-mode model have certain symmetries. For example, the equations are symmetric on the W_{101} – W_{011} subspace with the $\{x_1, x_2\} \rightarrow \{x_2, x_1\}$ transformation,⁵⁰ i.e., the reflection symmetry about the right diagonal ($x_1 = x_2$ line). However, the solutions have a broken symmetry. In Fig. 19, we show the fixed point solutions and the limit cycles on the W_{101} – W_{011} plane for (a) SQ (black dot), (b) ASQ (blue dot), (c) OASQ (red curve), and (d) SQOR (green curve). SQOR is symmetric under the $\{x_1, x_2\} \rightarrow \{x_2, x_1\}$ transformation. Other solutions do not have such symmetry.

However, each attractor has other sets of solutions, which can be found via different initial conditions. We show these sets of solutions as grey dots or curves in Fig. 19. These sets of solutions are related through symmetries. For example, all the solutions of the SQ fixed points (four solutions in the W_{101} – W_{011} plane) together show reflection symmetry about the axes and the diagonals. Similar kind of symmetry can be observed for ASQ, OASQ, and SQOR, when we consider all the possible solutions of these attractors.

Chaotic attractors *Ch1*, *Ch2*, *Ch3*, and *Ch4* have broken symmetry. However, in a statistical sense *Ch2* and *Ch4* have reflection symmetry about the axes and the diagonals. *Ch1* has reflection symmetry only about the diagonals, while *Ch3* has reflection symmetry only about the axes (see Fig. 5 of Pal *et al.*¹).

The wavy roll solutions show a trivial structure on the W_{101} – W_{011} plane as $W_{011} = 0$. However, phase space projec-

tion on the W_{101} – W_{111} subspace is non-trivial. The *Ch5* attractor shows possibilities of two different solutions ($\pm W_{101}$) accessible via different initial conditions. In statistical sense, each of the solutions are symmetric about the $W_{111} = 0$ axis (see Fig. 16). However, when we consider the set of both solutions, they show reflection symmetry (in a statistical way) about the $W_{101} = 0$ axis as well. In a similar way, the frequency locked state, quasi-periodic state, and periodic state of the wavy roll solutions show reflection symmetry about the axes. The *Ch6* attractor is a merged state of the *Ch5* attractors. Therefore, *Ch6* exhibits the reflection symmetry about both the axes in a statistical sense.

VII. CONCLUSION

In conclusion, we explored various flow patterns of zero-P convection and performed a detailed bifurcation analysis near the onset of convection using direct numerical simulation and a 27-mode low-dimensional model. The low-dimensional model was constructed using the most energetic modes of DNS. The results of the DNS and the low-dimensional model are in good agreement with each other. Several new chaotic attractors and windows of periodic and quasiperiodic rolls have been reported for the first time for zero-P convection. In Table I, we list all these patterns along with their range of r values as obtained in model and DNS. The origin and dynamics of all the observed patterns have been explained successfully using the bifurcation diagrams.

The RBC system for $P=0$ is chaotic at the onset itself with three qualitatively different attractors coexisting for a

TABLE I. Range of r values for various flow patterns in 27-mode model and DNS. For $Ch4$, we could not find an exact upper range of r values in DNS. However, it exists at least up to $r = 1.0342$.

Flow patterns/bifurcation points	r (model)	r (DNS)
SQ	1.690 – 1.2677	1.2006 – 1.4927
ASQ	1.1260 – 1.690	1.131 – 1.2005
NS1	~1.1245	~1.131
NS2	~1.1181	~1.1315
OASQ	1.086 – 1.1181	1.0709 – 1.1315
SQOR	1.0046 – 1.086	1.0048 – 1.0708
$Ch1, Ch2, Ch3$	1 – 1.0046	1 – 1.0048
$Ch4$	1 – 1.056	1 – 1.0342+
$Ch5, Ch6$	1 – 1.081	1 – 1.07
Quasiperiodic wavy rolls	1.081 – 1.116	1.07 – 1.095
Wavy rolls	1.116 – 1.503	1.095 – 1.6

given Rayleigh number. The stability analysis of the 27-mode model indicates three bifurcation points on the $r = 1$ plane that play critical roles in the dynamics of convection near the onset. The chaotic attractors $Ch1$, $Ch2$, and $Ch3$, described earlier by Pal *et al.*,¹ and $Ch4$ are all related to the bifurcation point CB3. Beyond $Ch1$ and $Ch4$, we observe SQOR, OASQ, ASQ, SQ, etc., which are common to Pal *et al.*'s 13-mode model. The other bifurcation point, CB2, is associated with the chaotic attractors $Ch5$ and $Ch6$ that are born from the periodic wavy roll solution through a quasiperiodic route to chaos. These patterns have been observed in earlier experiments and simulations. In addition, we find that the frequency of the previously observed wavy rolls is connected to the imaginary part of the eigenvalues of the stability matrix at the CB2 bifurcation point. Thus, the bifurcation analysis presented in the paper provides useful insights into the origin of the wavy rolls of RBC.

Interestingly, the bifurcation diagram of the 30-mode model of Mishra *et al.*¹⁷ for $P = 0.0002$ matches quite closely with Bif-A of our model. This reinforces earlier observations¹⁶ that zero- P convection is a valid limit of low- P convection as $P \rightarrow 0$. The extension of the present study to low- P convection in relation to wavy rolls will be very valuable for understanding the experimental and numerical findings near the onset.

ACKNOWLEDGMENTS

We are thankful to Stephan Fauve, Krishna Kumar, and Pankaj K. Mishra for useful discussions. This work is supported by the Swarnajayanti fellowship grant to M.K.V. by Department of Science and Technology, India. Some of the DNS runs were performed on PARAM YUVA for which we thank Centre for Development of Advanced Computing (CDAC).

- ¹P. Pal, P. Wahi, S. Paul, M. K. Verma, K. Kumar, and P. K. Mishra, *EPL* **87**, 54003 (2009).
- ²S. Chandrasekhar, *Hydrodynamic and Hydromagnetic Stability* (Cambridge University Press, Cambridge, 1961).
- ³F. H. Busse, "Transition to turbulence in Rayleigh-Bénard convection," in *Topics in Applied Physics: Hydrodynamic Instabilities and the Transition to Turbulence*, Vol. **45**, edited by H. L. Swinney and J. P. Gollub (Springer-Verlag, Berlin, 1981), pp. 97-137.
- ⁴J. K. Bhattacharjee, *Convection and Chaos in Fluids* World Scientific, Singapore, 1987.
- ⁵P. Manneville, *Instabilities, Chaos and Turbulence* Imperial College, London, 2004.
- ⁶G. Ahlers, S. Grossmann, and D. Lohse, *Rev. Mod. Phys.* **81**, 503 (2009).
- ⁷F. H. Busse, *J. Fluid Mech.* **52**, 97 (1972).
- ⁸R. M. Clever and F. H. Busse, *J. Fluid Mech.* **65**, 625 (1974).
- ⁹F. H. Busse and E. W. Bolton, *J. Fluid Mech.* **146**, 115 (1984).
- ¹⁰V. Croquette, *Contemp. Phys.* **30**, 113 (1989).
- ¹¹V. Croquette, *Contemp. Phys.* **30**, 153 (1989).
- ¹²M. C. Cross and P. C. Hohenberg, *Rev. Mod. Phys.* **65**, 851 (1993).
- ¹³E. Bodenschatz, W. Pesch, and G. Ahlers, *Annu. Rev. Fluid Mech.* **32**, 709 (2000).
- ¹⁴A. Das, U. Ghosal, and K. Kumar, *Phys. Rev. E* **62**, R3051 (2000).
- ¹⁵R. F. Stein and A. Norlund, *Sol. Phys.* **192**, 91 (2000).
- ¹⁶O. Thual, *J. Fluid Mech.* **240**, 229 (1992).
- ¹⁷P. K. Mishra, P. Wahi, and M. K. Verma, *EPL* **89**, 44003 (2010).
- ¹⁸M. Meneguzzi, C. Sulem, P. L. Sulem, and O. Thual, *J. Fluid Mech.* **182**, 169 (1987).
- ¹⁹R. M. Clever and F. H. Busse, *Phys. Fluids A* **2**, 334 (1990).
- ²⁰H. T. Rossby, *J. Fluid Mech.* **36**, 309 (1969).
- ²¹R. Krishnamurti, *J. Fluid Mech.* **42**, 295 (1970).
- ²²R. Krishnamurti, *J. Fluid Mech.* **60**, 285 (1973).
- ²³J. Maurer and A. Libchaber, *J. Phys. Lett.* **41**, 515 (1980).
- ²⁴A. Libchaber, C. Laroche, and S. Fauve, *J. Phys. Lett.* **43**, 211 (1982).
- ²⁵A. Libchaber, S. Fauve, and C. Laroche, *Physica D* **7**, 73 (1983).
- ²⁶G. E. Willis and J. W. Deardorff, *Phys. Fluids* **10**, 931 (1967).
- ²⁷F. H. Busse, and J. A. Whitehead, *J. Fluid Mech.* **66**, 67 (1974).
- ²⁸E. W. Bolton and F. H. Busse, *J. Fluid Mech.* **150**, 487 (1985).
- ²⁹F. B. Lipps, *J. Fluid Mech.* **75**, 113 (1976).
- ³⁰H. Ozoe and T. Hara, *Numer. Heat Transfer, Part A* **27**, 307 (1995).
- ³¹S. Fauve, E. W. Bolton, and M. E. Brachet, *Physica D* **29**, 202 (1987).
- ³²K. Kumar, S. Fauve, and O. Thual, *J. Phys. II (France)* **6**, 945 (1996).
- ³³K. Kumar, P. Pal, and S. Fauve, *Europhys. Lett.* **74**, 1020 (2006).
- ³⁴P. Pal and K. Kumar, *Phys. Rev. E* **65**, 047302 (2002).
- ³⁵D. R. Jenkins and M. R. E. Proctor, *J. Fluid Mech.* **139**, 461 (1984).
- ³⁶E. Knobloch, *J. Phys. II (France)* **2**, 995 (1992).
- ³⁷E. A. Spiegel, *J. Geophys. Res.* **67**, 3063 (1962).
- ³⁸C. Canuto, M. Hussaini, A. Quarteroni, and T. Zang, *Spectral Methods in Fluid Dynamics* (Springer-Verlag, Berlin, 1988).
- ³⁹See the animations Video-3 to Video-7 at http://turbulence.phy.iitk.ac.in/animations:convection#zero-p_convection.
- ⁴⁰K. Nandakumar and A. Chatterjee, *Nonlinear Dyn.* **40**, 149 (2005).
- ⁴¹P. Wahi and A. Chatterjee, *Int. J. Non-Linear Mech.* **43**, 111 (2008).
- ⁴²A. Dhooze, W. Govaerts, and Y. A. Kuznetsov, *ACM Trans. Math. Softw.* **29**, 141 (2003).
- ⁴³J. Guckenheimer and P. Holmes, *Nonlinear Oscillations, Dynamical Systems, and Bifurcations of Vector Fields* Springer-Verlag, Berlin, 1983.
- ⁴⁴Y. A. Kuznetsov, *Elements of Applied Bifurcation Theory* Springer-Verlag, Berlin, 1983.
- ⁴⁵R. C. Hilborn, *Chaos and Nonlinear Dynamics: An Introduction for Scientists and Engineers* Oxford University Press, Oxford, 1994.
- ⁴⁶G. E. Willis and J. W. Deardorff, *J. Fluid Mech.* **44**, 661 (1970).
- ⁴⁷V. Croquette and H. Williams, *Physica D* **37**, 300 (1989).
- ⁴⁸P. Ashwin, J. Buescu, and I. Stewart, *Phys. Lett. A* **193**, 126 (1994).
- ⁴⁹P. Ashwin, J. Buescu, and I. Stewart, *Nonlinearity* **9**, 703 (1996).
- ⁵⁰J. Moehlis, J. Porter, and E. Knobloch, *Physica D* **238**, 846 (2009).